# Thermal analysis and pack level design of battery thermal management system with liquid cooling for electric vehicles

Yoong Chung, Min Soo Kim*

*Department of Mechanical and Aerospace Engineering, Seoul National University, Seoul 08826, Republic of Korea*

ABSTRACT

In this paper, a comparative study for structural design of battery thermal management system is presented for electric vehicles. A thermal model for the pouch battery pack with liquid cooling is developed for thermal analysis of various pack designs. Typical battery pack with fin-cooling structure is set as a reference design, and thermal behavior of the battery pack is examined in the aspect of cooling performance and temperature uniformity. Numerical results indicate that poor heat conductivity from the bottom of the cell stack to the cooling plate is one of the major barriers to the efficient heat dissipation and asymmetric design of fin-cell arrangement have negative effect on the temperature uniformity of the battery pack. To improve the performance of the thermal management system, various structural designs are suggested and evaluated based on plural criteria. A new structural design for the large-scale battery pack is suggested to enhance the cooling performance and temperature uniformity of the battery pack minimizing the increase in system volume, weight, and pressure drop.

## 1. Introduction

Since the transport sector shares a large portion of the fuel consumptions and greenhouse gas emissions, electric vehicles (EVs) are widely accepted as promising alternatives to traditional automobiles [1]. Lithium-ion battery (LIB) is commonly regarded as a superb energy storage device in electric vehicles due to the adventurous features such as high power density, long cycle life, low self-discharge rate, and little memory effect [2]. However, the performance and reliability of the lithium-ion battery are highly dependent on its operation temperature [3]. While the cold operation of the battery causes low electrochemical reaction rate and reduced battery capacity [4], overheat of the battery expedites capacity degradation and may lead to thermal runaway [5]. For this reason, proper battery thermal management (BTM) is required to adopt the LIB in EV applications.

Battery thermal management systems for EV should meet the following conditions: (1) high cooling performance, (2) good temperature uniformity, (3) small BTM system size and weight. As the battery capacity is being increased in EV applications to extend the driving range, heat generation from the battery also becomes a severe issue. It is so especially for the fast charging conditions in which heat generation rate is steeply increased in proportion to the charging or discharging current. Thus, high cooling performance is crucial to enable the fast

charging of electric vehicles with large battery capacity. Temperature uniformity is as important as cooling performance or average temperature level of the battery. Non-uniform temperature causes incomplete energy utilization, uneven battery degradations, and even thermal runaway [6]. Size and weight of the BTM system need to be considered as well. Since the bulky and heavy battery packs have negative effects on the total battery capacity and driving range, compact and light BTM structures are required in EV applications.

To satisfy the conditions described above, many researchers have investigated the battery cooling system with various cooling strategies including air cooling, liquid cooling, and PCM cooling [7]. While air cooling is a simple way to cool down the battery pack, it is not suitable for the large-capacity battery pack in that air has low thermal conductivity and heat capacity. Han et al. [8] noted that the cooling capacity of the air is only a ninth of that of the water under the practical volume flow rate conditions. PCM cooling is one of the most effective ways to reduce temperature non-uniformity and prevent thermal runaway [9], and some drawbacks have been being overcome with recent developments including low thermal conductivity [10] and volume variations during the phase change [11]. Still, more progress is required for the cost of the total system to be widely adopted in electric vehicles. Meanwhile, the liquid cooling system is generally accepted as a promising and practical cooling strategy with compact design and superior

---

### Nomenclature

| | |
|---|---|
| $A$ | unit area [m$^2$] |
| $A_c$ | cross-section area of the coolant channel [m$^2$] |
| $A_s$ | suface area of the coolant channel [m$^2$] |
| $c_p$ | specific heat at constant pressure [J kg$^{-1}$ K$^{-1}$] |
| $D_h$ | hydraulic diameter [m] |
| $E$ | open circuit voltage [V] |
| $F$ | Faraday constant [s A mol$^{-1}$] |
| $f_{cool}$ | Darcy friction factor of working fluid [-] |
| $h_{cool}$ | convective heat transfer coefficient of working fluid [W K$^{-1}$ m$^{-2}$] |
| $I$ | current [A] |
| $L$ | length of coolant channel [m] |
| $\dot{m}$ | mass flow rate of coolant [kg s$^{-1}$] |
| $n$ | number of transferred electron |
| Nu | Nusselt number (Nu = $hL/k$) |
| Pr | Prandtl number (Pr = $c_p \mu/k$) |
| $\Delta P$ | pressure drop of the working fluid [kPa] |
| $\dot{Q}$ | heat generation/transfer rate [W] |
| $R$ | internal resistance [$\Omega$] |
| Re | reynolds number (Re = $\rho v D_h/\mu$) |
| SOC | state of charge |
| $\Delta S$ | entropy change [J K$^{-1}$ mol$^{-1}$] |

| | |
|---|---|
| $T$ | temperature [K] |
| $\bar{T}$ | average temperature [K] |
| $t$ | time [s] |
| $U$ | overall heat transfer coefficient [W m$^{-2}$ K$^{-1}$] |
| $\overline{UA}$ | equivalent heat conductance [W K$^{-1}$] |
| $V$ | operating voltage [V] |

*Greek symbols*

| | |
|---|---|
| $\rho$ | Density [kg m$^{-3}$] |
| $\gamma$ | aspect ratio of the coolant channel |

*Subscripts*

| | |
|---|---|
| *air* | airside |
| *cell* | lithium-ion cell |
| *cool* | working fluid |
| *gen* | heat generation |
| *irr* | irreversible heat generation |
| *rev* | reversible heat generation |
| *fn* | fin neck |
| *cp* | cooling plate |

cooling performance [12]. While water is commonly considered as the working fluid, concern about electrical short is a major barrier in the water cooling. Therefore, indirect liquid cooling method is adopted by many of the leading EV manufacturers such as Tesla, GM, and BMW [13].

Many studies about the liquid cooling system have focused on the component level approach, especially for the geometric optimization of the cooling plate and coolant channels. Jarrett et al. [14] noted that the optimal design of the cooling plate could be changed according to the targeting parameters: average cell temperature, temperature deviation, and coolant pressure drop. Other researchers have also studied the effect of the geometric modification of the cooling plate including serpentine channel [15], cross-area shape [16], and the number of the parallel coolant channels [17,18]. Jin et al. [19] developed an ultra-thin cooling plate with mini channels and experimentally suggested overall heat transfer coefficient of the plate. Chen et al. [20] compared various inter-cell structures for liquid cooling such as metal fin, water jacket, and direct liquid contact. The result shows that jacket cooling shows the highest cooling performance and minimum power consumptions compared to other methods. However, it is also noted that jacket cooling is not good for the temperature uniformity due to the relatively long flow path. Han et al. [8] developed a parameter that quantitatively presents the cooling performance of the battery pack with various cooling strategies.

However, those studies for the liquid-cooled battery packs mainly adopted component level approach with a specific battery pack design. Thus, only a few papers have focused on the system level approach considering structural designs of the large-scale battery pack. However, it is noted that average temperature and temperature deviations can be highly affected by the structural design [21], and it becomes more crucial for the large-scale battery pack. Zhao et al. [22,23] attempted to investigate the thermal behavior of the practical large-scale battery pack with liquid cooling, and found that optimization of the structural design such as orderly magnified contact angle and multiple short channel design could reduce the thermal non-uniformity. Shang et al. [24] optimized the structure and operation conditions of the prismatic battery pack applying the orthogonal test of several design parameters. Yeow et al. [25] addressed the effect of the dual cold plate on the thermal behavior of indirect fin-cooling battery pack. They found that

the location of the cold plate largely affects the temperature distribution, and direction of coolant flow has a significant impact on the maximum temperature difference. However, all those structural developments also have drawbacks such as extra system pressure drop, or system volume and weight increase. Therefore, it is required to evaluate the various structural designs of battery thermal management system with well-organized plural criteria that present the pros and cons of each design, and finally to suggest the optimal structural design that minimizes the drawbacks.

Aiming the structural design optimization of the BTM system with indirect fin-cooling method, which is one of the most widely adopted methods in EV applications, this study conducted a comparative study of various structural designs for the BTM systems with well-organized parameters to diagnose the systems. A computationally efficient numerical model is developed to investigate thermal behavior and features of each battery pack design. At first, a typical battery pack design is set as a reference model, and structural features that affect the cooling performance and temperature uniformity are investigated. The equivalent heat conductance is firstly introduced to the numerical study to quantify the cooling performance, and temperature uniformity is further analyzed with three temperature deviation factors; inner-cell, inter-cell, and inter-stack deviation. Based on the results for the reference model, two strategies are investigated including alternative combinations of battery stacks and cooling plates, and symmetric stack arrangement. All the suggested structural designs are compared and evaluated based on plural criteria such as the equivalent heat conductance, maximum temperature difference, volume and weight increase, and total system pressure drop.

## 2. Model description

### 2.1. Heat generation of lithium-ion cell

A commercial pouch-type lithium polymer cell with NMC (Nickel-Manganite-Cobalt) cathode and graphite anode is considered as a target battery cell in this work. Size of the battery cell is 200 mm × 100 mm × 8 mm, and the capacity of the cell is 16 Ah. Inside the battery is a layered structure of porous materials including the anode electrode, separator, and cathode electrode. The porous

structure is filled with electrolyte, and the cell is sealed with laminated film.

It is known that heat generation from the lithium-ion battery consists of two part: irreversible heat from the internal resistance of the cell and reversible heat by the entropy change [26] as presented in Eq. (1).

$$\dot{Q}_{gen} = \dot{Q}_{irr} + \dot{Q}_{rev} = I(E - V) + IT\frac{dE}{dT} = I^2R - T\Delta S\frac{I}{nF} \tag{1}$$

where $R$, $\Delta S$, and $F$ denote internal resistance, entropy change, and Faraday constant respectively. Relations for the internal resistance and the open circuit voltage are founded by applying linear relation of cell operating voltage and current ($V = E - IR$) to the experimental data presented by Vanquez-Arenas et al. [27]. For example, Eqs. (2) and (3) respectively show the relations of SOC to internal resistance for the charging and discharging procedures.

$$R_{charge} = (7.46E - 3)\cdot\exp((-2.19E - 1)\cdot SOC) + (6.89E - 4)$$
$$\cdot\exp((2.49E - 0)\cdot SOC) \tag{2}$$

$$R_{discharge} = (6.17E - 3)\cdot\exp((-6.23E - 0)\cdot SOC) + (1.01E - 2)$$
$$\cdot\exp((-1.72E - 1)\cdot SOC) \tag{3}$$

Entropy change for the NMC-graphite LIB is presented by Viswanathan et al. [28]. Detailed descriptions and validations of the battery cell model are presented in Appendix A.1. Considering a quick charging condition with 2 C-rate, which is a harsh condition with a large amount of heat generation, average heat generation rate is about 9.6 W. In this study, simulation is carried out for both transient heat generation and average constant heat generation conditions. The former is to examine the actual thermal behavior of the battery pack under quick charging conditions, and the latter is to estimate and analyze the thermal performance of the battery pack under a certain heat generation level.

### 2.2. Governing equations

Fig. 1 shows the schematics of a practical and typical battery pack structure with metal fins and cooling plates. Thin cooling fins with aluminum alloy are inserted in every cell spacing to dissipate the generated heat to the cooling plates. In order to protect, insulate, and fix the pouch cell bodies, each cell is covered with an insulating case except for the surface faced with metal fin. As pouch cells are sealed with the laminated film, edges of the cells are not perfectly contacted with the case, and air gap hinders the heat transfer. Cooling plate is

located beneath the cell stack and has four straight sub-channels with square cross-sections. Thermally conductive pad is employed to reduce the contact resistance between the cell stack and cooling plate and to insulate the battery stack.

In the numerical model, simulation domain is divided into two parts; cell stack structure and coolant channel. The energy conservation equation of the cell stack structure is presented as

$$\rho c_p \Delta V \frac{\partial T}{\partial t} = \Delta (UA)_x \frac{\partial T}{\partial x} + \Delta (UA)_y \frac{\partial T}{\partial y} + \Delta (UA)_z \frac{\partial T}{\partial z} + \Delta \dot{Q}_{gen} \tag{4}$$

Focusing on the pack-level analysis, uniform thermal and electrical property assumptions are adopted inside the cell following the precedent studies [22–24]. Due to the layered structure, the equivalent thermal conductivity of the cell is obtained differently depending on the direction. The battery pack is regarded to be adiabatic except for the heat dissipation through the coolant flow as presented in Eq. (5).

$$\frac{dT}{dx}\bigg|_{x=0} = \frac{dT}{dx}\bigg|_{x=W_{stack}} = \frac{dT}{dy}\bigg|_{y=H_{stack}} = \frac{dT}{dz}\bigg|_{z=0} = \frac{dT}{dz}\bigg|_{z=L_{stack}} = 0$$
$$\Delta (UA)_{y=0}\frac{dT}{dy}\bigg|_{y=0} = \Delta \dot{Q}_{trans} \tag{5}$$

where $x$, $y$ and $z$ respectively denote the direction along the stack width, height and length. Thermal conduction and heat capacity of the electric connections such as terminal connections, welding tab, and plastic holder are not considered as those are negligible in the thermal model. Thermal properties of all the components are summarized in Table 1.

For the working fluid, flow distribution to the straight sub-channel is assumed to be uniform and 1-D energy conservation equation is adopted in the channel flow calculation in order to efficiently calculate the thermal behavior of large-scale battery packs. Therefore, the energy conservation equation of the coolant channel is presented as

$$\rho_{cool} c_{p,cool} A_c \frac{\partial T}{\partial t} = \dot{m} c_{p,cool} \frac{\partial T}{\partial l} + \frac{d\dot{Q}_{trans}}{dl}$$
$$= \dot{m} c_{p,cool} \frac{\partial T}{\partial l} + h_{cool} \Delta A_s (T_{cp} - T_{cool}) \tag{6}$$

As the channel length is much larger than channel cross-area, the working fluid is mostly under the fully-developed state in the straight sub-channels. Gnielinski correlation [29] is applied to obtain the convective heat transfer coefficient under the conditions as follows.

$$Nu_{cool} = \frac{(f_{cool}/8)(Re_{cool} - 1000)Pr_{cool}}{1 + 12.7(f_{cool}/8)^{0.5}(Pr_{cool}^{0.66} - 1)}, \quad 2300 < Re_{cool} < 5 \times 10^6 \tag{7}$$
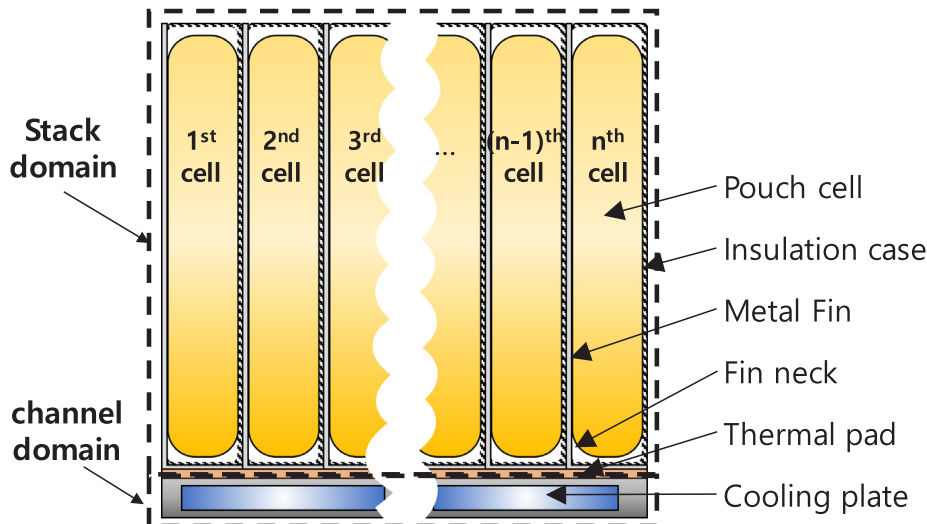


**Fig. 1.** Typical structure of battery stack with metal fin and cooling plate.

**Table 1**
Thermal properties of the BTM (Battery thermal management) system.

| Material | $\rho\,[\text{kg}\cdot\text{m}^{-3}]$ | $c_p\,[\text{J}\cdot\text{kg}^{-1}\cdot\text{K}^{-1}]$ | $k\,[\text{W}\cdot\text{m}^{-1}\cdot\text{K}^{-1}]$ |
|---|---|---|---|
| Aluminum alloy | 2700 | 893 | 170.0 |
| Thermal pad | 3100 | 930 | 5.0 |
| Insulation case | 2300 | 1430 | 1.5 |
| Battery cell | 1780 | 1000 | 30/0.5 (in/cross-plane) |

$$f_{cool} = (1.0875 - 0.1125\gamma)\cdot f_{cool,0} \tag{8}$$

where $f_{cool,0}$, and $\gamma$ respectively denote the friction factor for circular duct and aspect ratio of rectangular channels [30]. Total pressure drop of the battery pack is calculated by adding friction loss from all the coolant path components including straight sub-channels, flow distributing/combining structures at the entrance and exit side of the cooling plate, and connecting tubes as presented in Eq. (9).

$$\Delta P = \sum_{i=1}^{n} f_{cool}\rho_{cool}(L/D)_{eqv}\frac{v_{cool}^2}{2} \tag{9}$$

where $(L/D)_{eqv}$ denotes the equivalent ratio of channel length to diameter, which is varied with the geometry of the component. To ensure the uniform flow distribution assumptions and equivalent ratio values of each component, further validation is presented with CFD simulations in Appendix A.2. Water is employed as working fluid.

### 3. Simulation results for reference pack design

Typical battery pack design is set as a reference model in this study. Fig. 2(a) shows reference design of a battery pack with a capacity of 9 kWh. The battery pack consists of 3 cell-fin stacks and each stack has 48 pouch cells. Total 144 cells are placed as presented in Fig. 2(b). Cooling plates are laid beneath the battery stack in the cross direction, and each plate has four cooling channels. As seen in the figures, inlet coolant flow is divided into 4 channels in the plate, and then merged again between the plates. Geometric specification of the battery pack is summarized in Table 2.

Firstly, grid independent test is done to ensure the validity of the simulation model. Numerical results after 2 C-rate charging simulation is presented according to the grid number per cell in Fig. 3. Simulation results are obtained under the grid number of 3200 for a cell. Fig. 4 shows simulation results for the temperature behavior of the reference battery pack with different charging rate. Average temperature and maximum temperature difference are obtained only from the pouch

**Table 2**
Specifications of the BTM system.

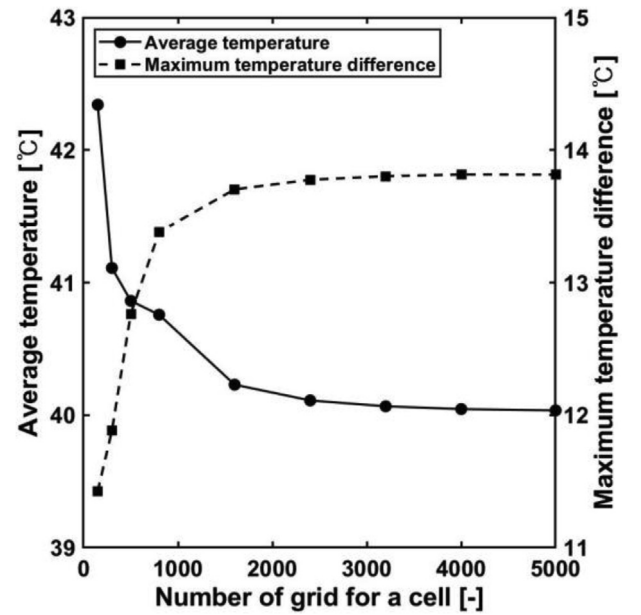| Component | Specifications |
|---|---|
| Pouch cell | Width (mm): 209<br>Height (mm): 107<br>Thickness (mm): 8 |
| Metal fin | Material: Aluminum 6061<br>Thickness (mm): 0.4<br>Fin neck to fin base (mm): 5 |
| Cooling plate | Material: Aluminum<br>Thickness (mm): 10<br>Channel height (mm): 6<br>Channel width (mm): 20 |
| Thermal pad | Thickness (mm): 2 |
| Battery pack | Cell number: 144<br>Total width (mm): 408<br>Total height (mm): 129<br>Total length (mm): 697 |



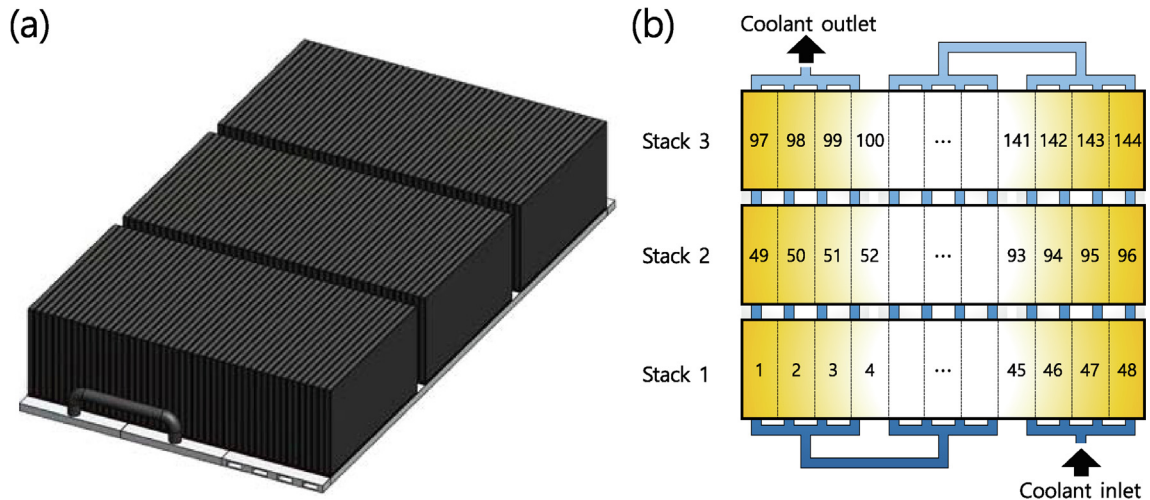**Fig. 3.** Grid independent test for the thermal model.



**Fig. 2.** (a) 3D geometry and (b) cell arrangement of reference battery pack.
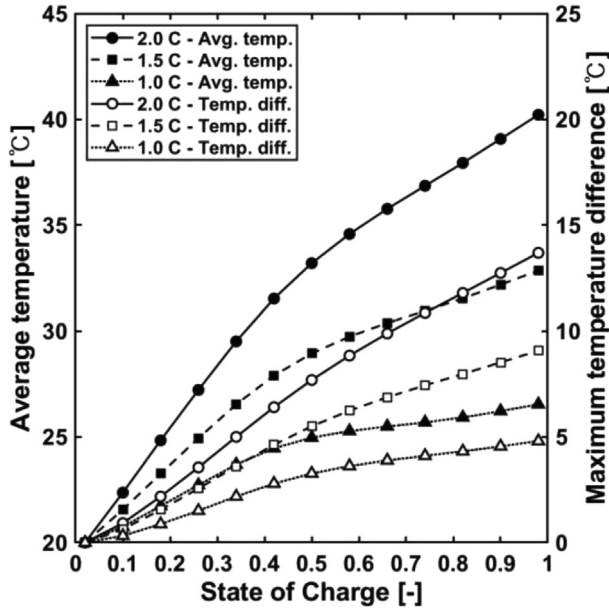
**Fig. 4.** Thermal behavior of the reference battery pack with different charging rate.

cells with a total number of 144, excluding other components such as metal fins and cooling plates. Especially, maximum temperature difference denotes the difference of the maximum temperature and minimum temperature at any location inside the pouch cells for the time. Initial temperatures of the battery pack and cooling plates are set to 20 °C. The inlet temperature of the coolant flow is also 20 °C, and inlet mass flow rate is set to 10 L/min. For lithium-ion battery, It is recommended to maintain the operating temperature in the range of 15 °C to 30 °C [31], and the maximum temperature difference under 5 °C [32]. This is well-maintained under low C-rate conditions. However, the average temperature exceeds 40 °C when the battery pack is charged for 2C-rate, and maximum temperature difference also shows bad results under high C-rate conditions. Considering the results, it is noted that the thermal performance of the battery pack requires to be improved in both cooling performance and temperature uniformity.

Path of the heat transfer from the cell body to the coolant is graphically summarized in Fig. 5. As the heat of the battery stack is mostly dissipated through the cooling fin, the path of the heat transfer can be divided into three sections following the figure; cell body to fin neck, fin neck to cooling plate, and cooling plate to coolant flow. Fin neck is the lowest point of the contact surface between the metal fin and pouch cell, where most of the heat is converged. To examine the cooling performance of the battery pack design in detail, the average temperature of each part of the battery pack is roughly calculated under the constant heat generation conditions. Using the average temperature results, the equivalent heat conductance, $UA$ is introduced to quantify the cooling performance of the reference design from the temperature distribution results. The equivalent heat conductance for the total BTM system can be calculated as

$$\bar{UA}_{total} = \frac{\dot{Q}_{total}}{(\bar{T}_{cell} - \bar{T}_{cool})}$$ (10)

Moreover, sectional $\bar{UA}$ is also derived following the path of the heat transfer. Relations between the sectional $\bar{UA}$ are presented as

$$\bar{UA}_{total}(\bar{T}_{cell} - \bar{T}_{cool}) = \bar{UA}_1(\bar{T}_{cell} - \bar{T}_{fn}) = \bar{UA}_2(\bar{T}_{fn} - \bar{T}_{cp})$$
$$= \bar{UA}_3(\bar{T}_{cp} - \bar{T}_{cool})$$ (11)

where $\bar{UA}_1$, $\bar{UA}_2$, and $\bar{UA}_3$ are for the sectional $\bar{UA}$ of the path 1, 2, and 3, respectively. Calculation results are summarized in Table 3. In short,

sectional $\bar{UA}$ shows how much the each part contributes to the thermal resistance of the battery structures. As seen in the table, $\bar{UA}_3$ has the largest value. It means that the convective heat transfer coefficient of the coolant makes little contribution to the thermal resistance of the battery pack with the sufficient flow rate of the working fluid. While the poor thermal conductivity of the pouch cell in the cross-plane direction has a negative effect on $UA_1$ value, thin and wide shape of the pouch cell helps heat dissipation to the stack bottom. However, $\bar{UA}_2$ value shows that a lot of thermal resistance occurs between the battery stack and cooling plate in spite of the short distance between the fin neck to the cooling plate. There are two reasons for that. Firstly, since the cooling fin has a very thin thickness in order to reduce the total volume of the battery pack, this bottleneck geometry causes an adverse effect on the heat conductance. In addition, while the thermally conductive pad is essential to reduce the contact resistance, it becomes extra thermal resistance with low conductivity of the pad itself. The thermal pad takes about 24% of the total thermal resistance between the fin neck and cooling plates. Considering the results, it is required to enhance the heat conductance between the battery stack and cooling plate, or increase the total heat transfer area to improve the cooling performance.

Fig. 6 shows the temperature distribution of the stack 1. The dotted line denotes the location of the cooling fin. While the maximum temperature is obtained at the right and top side of the battery pack, the minimum temperature is recorded at the left and bottom side of the battery pack. Reason for the temperature gradient in the vertical direction is the heat transfer from the battery cell to the cooling plate. However, the temperature gradient also occurs in the horizontal direction. It is because of the asymmetric arrangement of the battery stack in the reference model. As the cooling plate is attached in the left side of the pouch cell, generated heat from the right-end cell is only dissipated to the left side, and left-end cooling fin has no heat transfer from the left side. This difference makes the heat dissipation easier at the left-end side, and harder at the right-end side.

This temperature deviation can be divided into three types; inner-cell deviation, inter-cell deviation, and inter-stack deviation. In order to reduce the maximum temperature difference, Contribution of each term should be calculated. Firstly, the mean values of the inner-cell temperature difference for all 144 cells is 6.47 °C. Fig. 7 shows the average temperature for each of the battery cells. The graph shows more clearly that not only the inner-cell temperature deviation but also the inter-cell temperature deviation takes quite a large portion of the temperature non-uniformity. For 3 battery stacks average inter-cell temperature deviation is 9.08 °C. Except for the end-side, mid-side temperature deviation is less severe. The stair-shaped temperature deviations in the
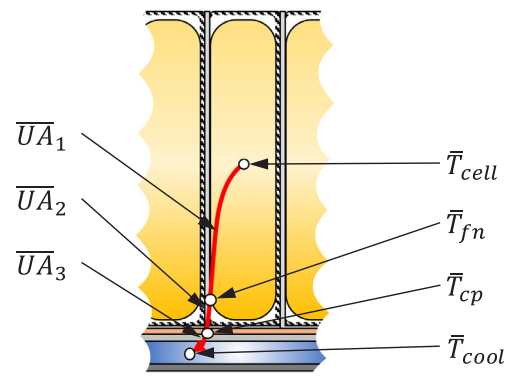


**Fig. 5.** Path of the heat transfer in the battery pack.

**Table 3**
Sectional equivalent heat conductance ($\overline{UA}$) for the reference design.

| Sectional $\overline{UA}$ | Value [W·K$^{-1}$] |
|---|---|
| Total | 22.0 |
| Cell body to fin neck (stack bottom) | 61.6 |
| Fin neck to cooling plate | 51.5 |
| Cooling plate to coolant flow | 102.2 |

mid-sides are due to the coolant flows beneath the stack. Inter-stack deviation also contributes to the maximum temperature difference of the battery pack. The temperature difference for the total battery pack is 0.43 °C bigger than the average temperature difference for each battery stack. As the heat dissipation through the airside is not considered in the model, this inter-stack temperature deviations between the battery stacks are entirely regarded with channel connections of the coolant flow. Consequently, temperature non-uniformity occurs from various reasons including stack arrangement, stack and cooling plate dispositions, and channel connections.

## 4. Comparison of the various pack-level designs

### 4.1. Alternative structures with different disposition of battery stack and cooling plate.

Since the path of the heat transfer from the stack bottom to the cooling plate highly contributes to the thermal resistance of the battery pack structure, several modified pack designs are devised to enhance the cooling performance. These are four different pack designs including the reference design.

(A) Reference design
(B) Thickened cooling fin design
(C) Sandwich cooling plate design
(D) Interspersed cooling plate design

Simply employing the thickened metal fin is one of the easy solutions to improve cooling performance. Type B has a similar geometric design with the reference model, but it has twice thicker cooling fin. As a substitute, cooling plates can be employed to the top side as well as the bottom side of the battery stack. Fig. 8(a) shows sandwich shaped battery pack design of the type C. Battery stacks are inserted between the cooling plates so that the generated heat is removed to both sides of the stack. Channel connections are designed considering the minimum system pressure drop. However, type C requires twice the cooling plates compared to the reference model. As the system pressure drop becomes larger and weight becomes heavier with extra cooling plates, this is a

clear disadvantage in the aspect of the total pressure drop of the working fluid and weight and size of the battery pack. In additions, as the coolant channel is located at the upper side of the battery stack, type C might be vulnerable to the leakage problems. Therefore, interspersed design of type D is devised in this paper to minimize the drawbacks by applying the both-side cooling structure. Instead of the horizontally laid long battery stack, the stack is partially divided and vertically laid as seen in Fig. 8(b). Small battery stacks and vertical cooling plates are alternatively located so that the coolant channels get heat from both sides of the cooling plates. By sharing the cooling plates, the total number of cooling plates can be reduced.

Fig. 9 shows the thermal behavior of the four battery pack designs under the 2 C-rate fast charging condition. Simulation conditions including the initial temperature, inlet coolant temperature, coolant mass flow rate, and channel connections are the same following Section 3. While type B shows improvement in cooling performance, temperature uniformity is still similar with the type A. Even though the thickened fin enhances the cooling performance in type B, it makes no structural changes to relieve the non-uniformity in the vertical direction. Type C and D similarly have the highest cooling performance and temperature uniformity. In terms of cooling plates being located on both sides of the battery stacks, those two designs are basically identical except for the number of the cooling plate and channel connections, which explains the similar thermal behavior. As the generated heat is removed through both top and bottom side cooling plates, the temperature gradient in the vertical direction is considerably reduced, and thus the temperature uniformity is improved.

The cooling performance of each battery pack design can be estimated quantitatively by calculating equivalent heat conductance. However, volume and mass of the battery pack should be considered as well as the cooling performance to employ the optimum battery pack design. Therefore, the ratio of the equivalent $UA$ value to the BTM system volume or weight is calculated for the constant heat generation conditions. When calculating the volume and weight of the battery pack, the portion of the battery cell itself is not counted to clearly show the results. The results are presented in Table 4. Despite the similar cooling performances of type C and D, type D has the highest score considering volume and mass increase with the less number of the cooling plates. It means that a larger number of LIB cell can be employed under the same volume and mass condition with type D. Results for the temperature deviations are also summarized in Table 4. It is noted that Type C and D shows much smaller inner-cell deviation as a result of the both-side cooling. More ever, the inter-cell deviation is also reduced because of the overall improvement of the cooling performance. The inter-stack deviation appears to be increased in type D, but this is a result of dividing a stack into three sub-stacks, which transfers the stair-shaped inter-cell temperature variance into the inter-stack
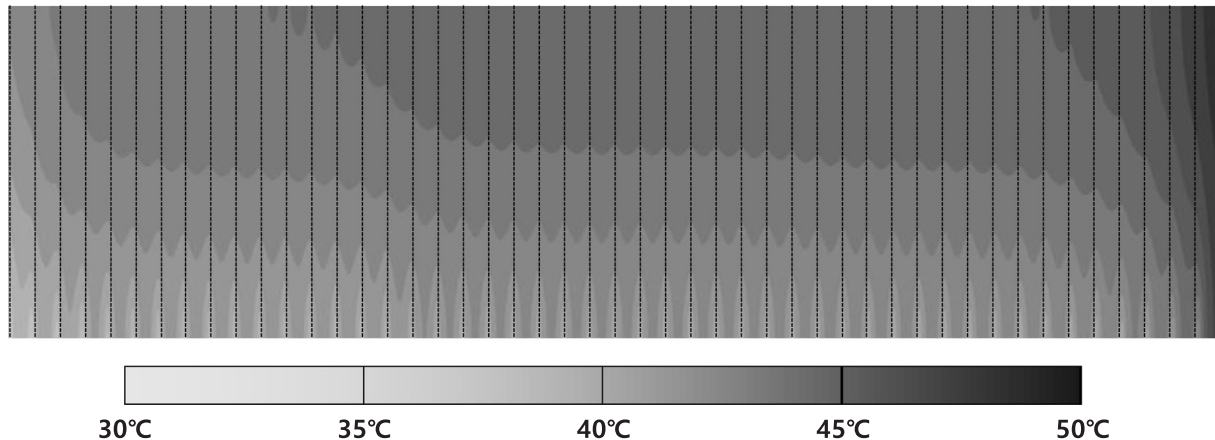


**Fig. 6.** Temperature distribution of reference battery pack, stack 1 (7500 Grid for a cell).
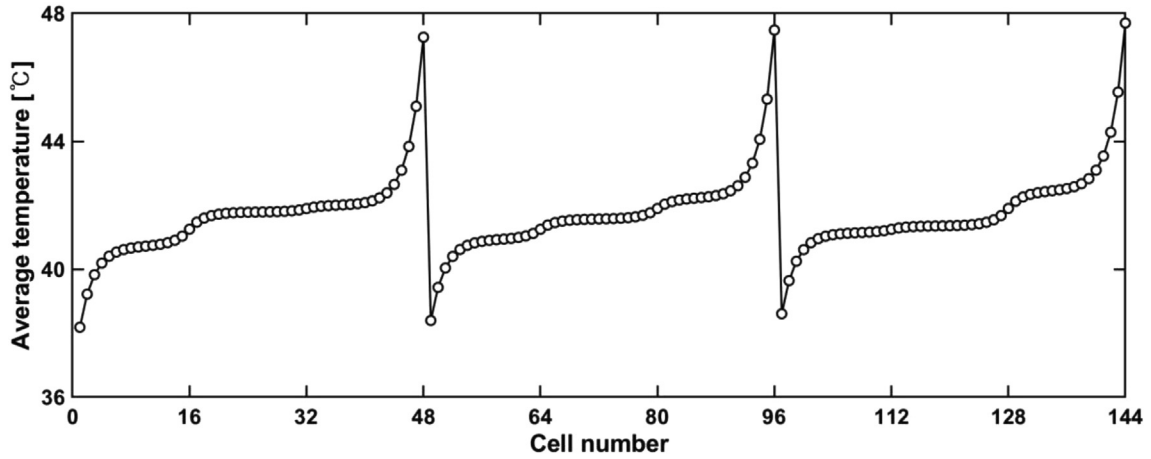
Fig. 7. Average cell temperature of reference battery pack.

deviation.

Since the total pressure drop of the working fluid is crucial to the operating power consumption, it is computed for the different structural designs. As the geometry of the coolant path for the type B is almost the same with type A, pressure drop variations according to the volume flow rate are presented for type A, C, and D in Fig. 10. Type C has the largest pressure drop with a relatively long distance of the coolant path. While type C requires a double number of cooling plates than reference type, type D needs only one more cooling plates to achieve both-side cooling. Thus, by reducing the number of cooling plates and U-type connecting tubes, type D can minimize the increase of the total pressure drop from the design modification. In addition, this

advantage becomes more highlighted as the scale of the battery pack increases in that extra pressure drop from the one extra cooling plate is diluted with larger number of the total cooling plates.

### 4.2. Symmetric stack arrangement

As some of the inter-stack temperature deviations come from the asymmetric arrangement of the battery stack, non-uniformity remains in spite of the improved battery pack designs. To solve this problem, a symmetric stack arrangement is suggested in Fig. 11. While each of the cooling fins is only faced with one battery cell in the asymmetric design, two battery cells are installed at both sides of the cooling fin in the
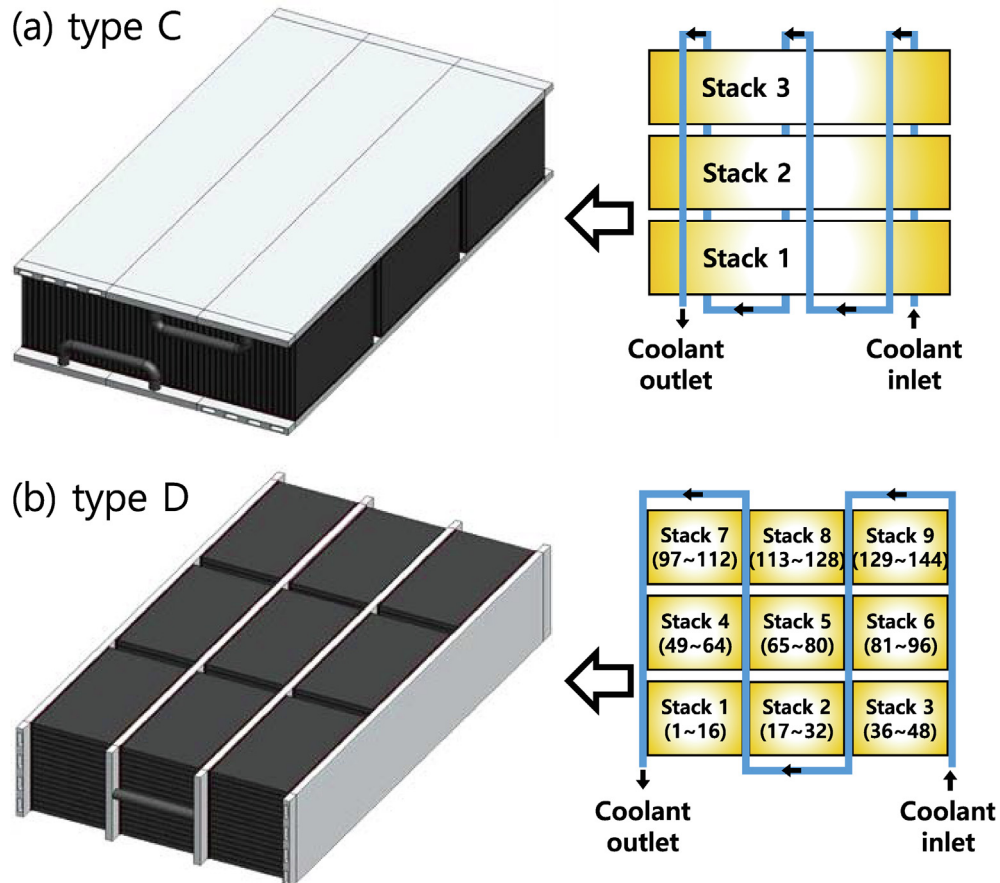


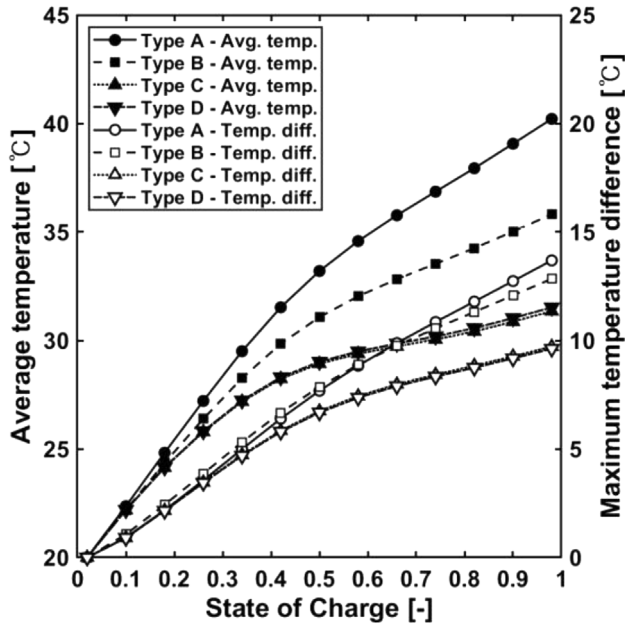Fig. 8. 3D geometry and channel connections of (a) type C and (b) type D.

**Fig. 9.** Thermal behavior of various battery pack designs.

**Table 4**
Comparison of different battery pack designs.

| Designs | Type A-1 | Type B-1 | Type C-1 | Type D-1 |
|---|---|---|---|---|
| $\overline{UA}$ to mass ratio [W·K$^{-1}$·kg$^{-1}$] | 4.86 | 5.04 | 6.74 | 7.96 |
| $\overline{UA}$ to volume ratio [W·K$^{-1}$·L$^{-1}$] | 9.99 | 11.01 | 14.31 | 16.63 |
| $\Delta T_{inner-cell}$ [K] | 6.47 | 5.32 | 2.06 | 2.86 |
| $\Delta T_{inter-cell}$ [K] | 9.08 | 7.87 | 6.58 | 5.29 |
| $\Delta T_{inter-stack}$ [K] | 0.43 | 0.43 | 0.04 | 1.25 |
| $\Delta T_{max}$ [K] | 16.8 | 14.1 | 9.59 | 9.49 |
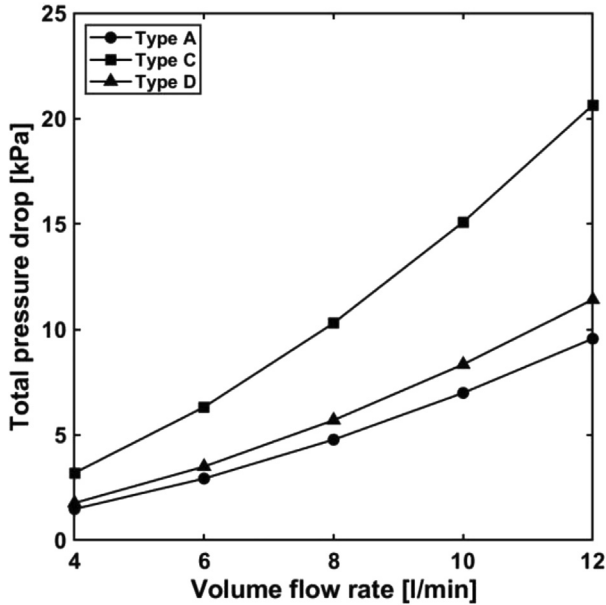


**Fig. 10.** System pressure drop of various battery pack designs according to volume flow rate change.

symmetric design. Since the number of the cooling fin becomes halved, the thickness of each cooling fin becomes twice in return. Fig. 12 shows the thermal behavior of the battery pack designs with symmetric stack arrangement for the fast charging condition. The opposite results are
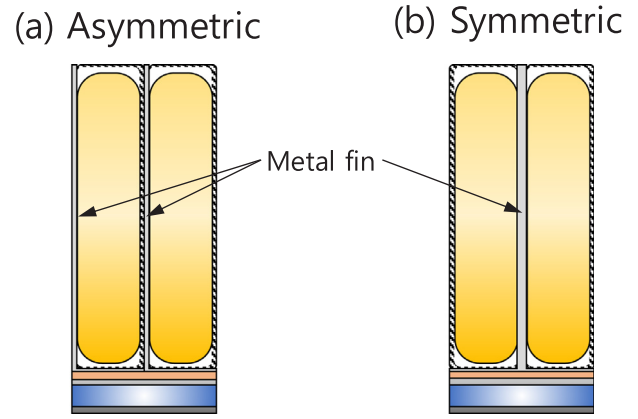


**Fig. 11.** Structure of battery stack with (a) asymmetric arrangement and (b) symmetric arrangement.

observed for the cooling performance and temperature uniformity when employing the symmetric stack arrangement. While the average temperature becomes slightly higher for all the designs, the maximum temperature difference is highly reduced with the symmetric stack arrangement. As the battery cells put their backside together in the symmetric design, less heat is dissipated through the backside of the battery cell. Therefore, symmetric stack arrangement is slightly disadvantageous in terms of cooling performance. However, side-end temperature imbalance is diminished by employing the symmetric stack arrangement except for the effect of the ambient temperature, and coolant flow temperature distributions. Fig. 13 compares the average temperature of each of the battery cells for type D with asymmetric and symmetric stack arrangements. This graph directly shows the pros and cons of the symmetric design. While the average temperature is increased by 1.13 °C, the maximum temperature difference is reduced by 4.1 °C.

Simulation results including the equivalent heat conductance and temperature deviations are computed for the symmetric designs as well in Table 5. Similar to the results for the asymmetric designs, type D shows the highest cooling performance with respect to the size and weight of the battery pack. The heat conductance values of the
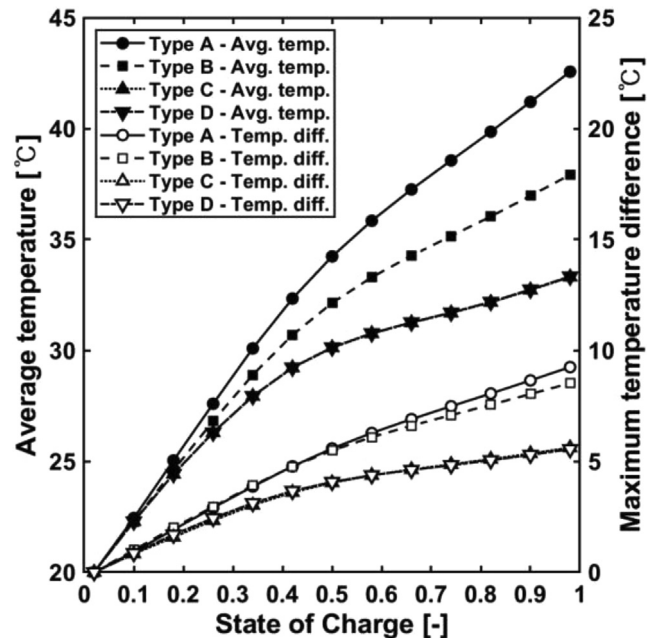


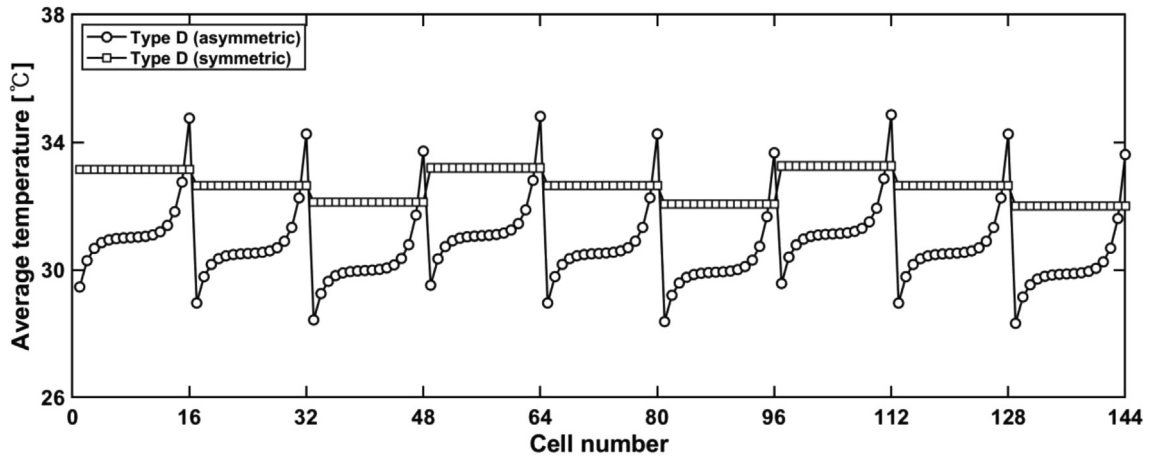**Fig. 12.** Thermal behavior of various battery pack designs (symmetric stack arrangement).

**Fig. 13.** Average cell temperature of battery pack for type D.

**Table 5**
Comparison of different battery pack designs with symmetric arrangement.

| Designs | Type A-2 | Type B-2 | Type C-2 | Type D-2 |
|---|---|---|---|---|
| $\bar{UA}$ to mass ratio [W·K$^{-1}$·kg$^{-1}$] | 4.13 | 4.28 | 5.56 | 6.70 |
| $\bar{UA}$ to volume ratio [W·K$^{-1}$·L$^{-1}$] | 8.51 | 9.35 | 11.8 | 14.0 |
| $\Delta T_{inner-cell}$ [K] | 9.23 | 7.47 | 4.13 | 4.72 |
| $\Delta T_{inter-cell}$ [K] | 1.29 | 1.31 | 1.31 | 0.01 |
| $\Delta T_{inter-stack}$ [K] | 0.43 | 0.43 | 0.04 | 1.25 |
| $\Delta T_{max}$ [K] | 10.95 | 9.21 | 5.47 | 5.35 |

symmetric designs are slightly smaller than those of the asymmetric designs regardless of the types. Despite the small disadvantages in cooling performance, it is inevitable to adopt the symmetric designs to achieve good temperature uniformity. Consequently, considering the cooling performance, temperature uniformity, and unintentional drawbacks, type D-2 is suggested as an alternative design for the reference design. Compared to the reference model, it shows the 38% improvement in the aspect of $\bar{UA}$ to volume ratio, and the maximum temperature difference is also reduced by 11.4 °C. More specially, Inter-cell deviation is reduced by 9.1 °C with the symmetric arrangement, and inner-cell deviation is reduced by 2.80 °C with the enhanced cooling performance.
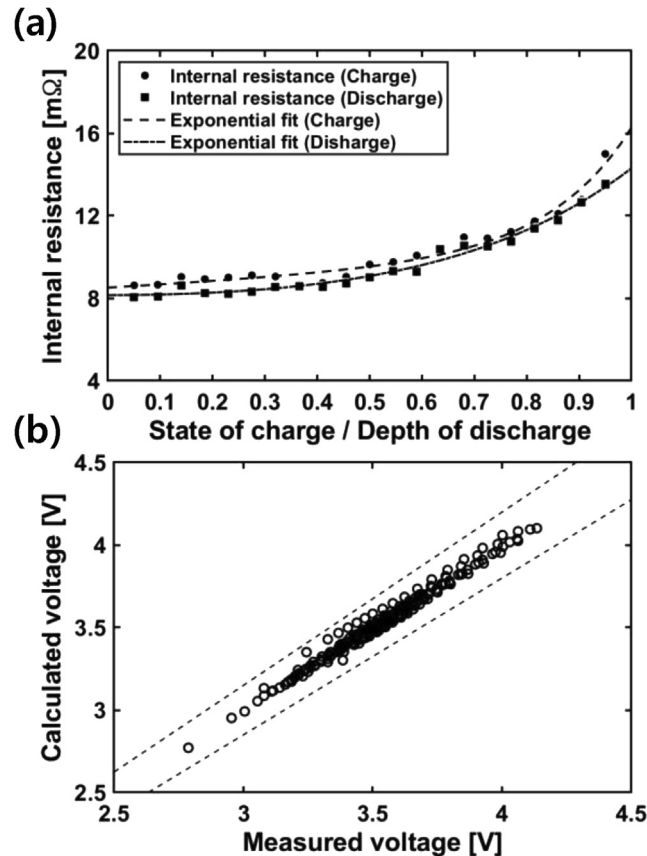


**Fig. 14.** (a) Internal resistance variations according to SOC (for charge) and DOD (for discharge), and (b) comparison of the simulation and experimental results of operating voltage.
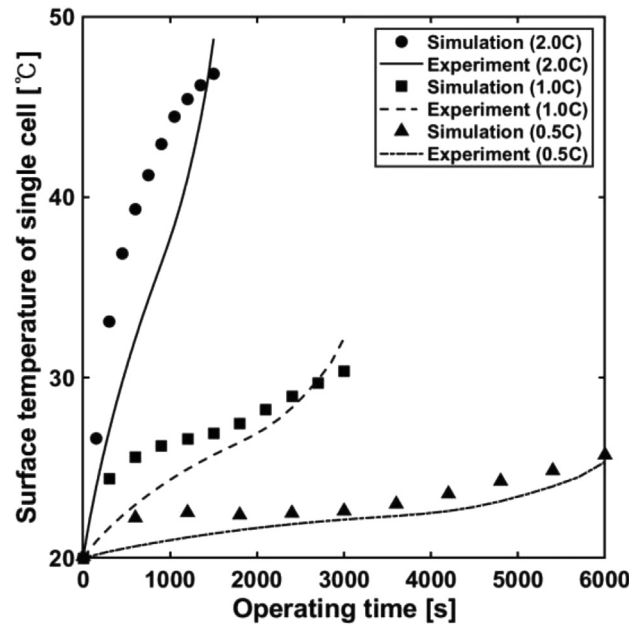
**Fig. 15.** Time-variations of the surface temperature for a single cell according to different C-rate conditions.
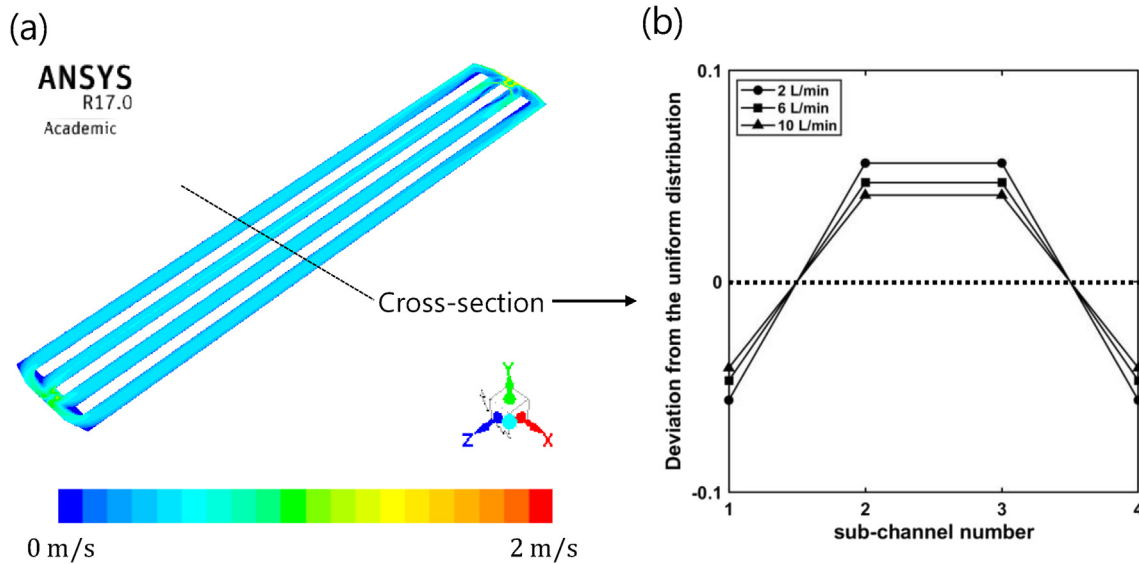


**Fig. 16.** (a) Flow velocity field of a cooling plate and entrance/exit structures and (b) deviation of the flow distribution to straight sub-channel from the uniform distribution.

**Table 6**
Equivalent ratio of the channel length to diameter.

| Component | $(L/D)_{eqv}$ |
|---|---|
| Straight sub-channel | 1.45e + 1 |
| Flow distributing structure | 3.58e + 1 |
| Flow combining structure | 1.02e + 2 |
| Straight connecting tube | 8.80e + 0 |
| U-type connecting tube | 4.81e + 1 |

## 5. Conclusion

This study is to optimize the structural design of the practical and large scale battery thermal management system for electric vehicles. A thermal model for the indirect fin-cooling battery pack is developed for this purpose.

A reference design is set to analyze the features that affect the cooling performance and temperature uniformity of the battery pack under quick charging condition. The equivalent heat conductance is introduced to quantify the cooling performance of the battery pack. It is shown that thermal resistance between the stack bottom to the cooling plate mainly contributes to the poor thermal conductance of the battery pack designs with metal fins and cooling plates. It is also noted that the inter-stack temperature deviation takes a large portion of total

temperature non- uniformity among the three deviation types due to the asymmetric stack arrangements.

As a result of a comparative study for the various battery pack designs, type D-2 is proposed as an alternative design for the BTM systems. Applying the structural type D, the ratio of the equivalent heat conductance to the system volume is improved by 64%. While the inner-cell and inter-cell deviations are largely reduced with the design modification as well, the total pressure drop is only increased by 19%. Adopting symmetric stack arrangement to type D (type D-2), the increase of the equivalent heat conductance to the system volume is reduced to 38%. However, the maximum temperature difference is reduced to 5.4 °C. While the inner-cell deviation is slightly increased with the symmetric design, reduction of the inter-cell deviation highly contributes to the improvement of the temperature uniformity.

The comparison results of the various battery pack structures in this paper can be applied to design the large-scale battery pack for electric vehicles. In particular, the newly proposed battery pack design is expected to significantly improve the thermal performance of the battery thermal management system. In future studies, the developed model also can be applied to analyze the various types of battery pack designs that are not suggested in this paper.

## Declaration of Competing Interest

The authors declared that there is no conflict of interest.

## Acknowledgments

## Appendix A

*Appendix A.1. Validation of electrical and thermal parameters of target cell*

This appendix is to provide a detailed description and validation for the electrical and thermal model of the target cell. Following the linear relation of operating cell voltage and cell current ($V = E - IR$), linear regression method is applied to voltage and current data under the CC charging/discharging experiments [27]. Fig. 14(a) shows the computed internal resistance and its fitting curve. However, as the experimental data is in the range of 0.125 to 1 C-rate, it is required to ensure the irrelevance of internal resistance to cell current. For this purpose, experimental results for the target cell are collected in a wide range of C-rate from other literature [33,34]. For the discharging conditions from 0.125 to 5 C-rate, computed voltage results are compared with measured voltage data in Fig. 14(b). The RMSE (Root mean square of error) is obtained as 0.030. The results show that the linear relation of the operating voltage and current is valid regardless of the C-rate.

Based on the specified electrical and thermal properties of the target cell, the thermal behavior of a single cell is predicted under various discharging C-rate conditions and compared with experimental data [33]. In the literature, a single cell is vertically fixed and exposed to the ambient air of 20 °C. Therefore, heat dissipation with natural convection is considered in the single cell model. Natural convective heat transfer coefficient is for the vertical plate is determined by Eq. (12) [35].

$$\bar{Nu}_{air} = \left\{ 0.825 + \frac{0.387 Ra^{0.167}}{[1 + (0.492/Pr)^{0.563}]^{0.296}} \right\}^2 \tag{12}$$

where Ra denotes Rayleigh number of the target system. Variations of the surface temperature over time according to different C-rates are presented in Fig. 15. In spite of the local errors, the simulation result shows a reasonable agreement to the actual thermal behavior of the single cell.

*Appendix A.2. Supplementary CFD simulations*

In order to validate the uniform flow distribution assumption, and compute the friction loss from the flow distributing/combining structures located at the entrance and exit of the cooling plates, CFD simulation is conducted with ANSYS/Fluent 17.0 for a cooling plate with flow distributing/combining structures as presented in Fig. 16(a). All the battery pack designs share this structure. Governing equations of the working fluid including mass, momentum, energy conservations are solved based on the precedent studies [36,37]. The k-epsilon model is adopted to solve the momentum equation, and the mesh convergence is ensured under the 3-D element number of $1.41 \times 10^7$. Fig. 16(b) presents deviation of the flow distribution from the perfectly uniform distribution for the straight sub-channels, which is one-fourth of total flow rate in this case. the maximum error is recorded as under 6%. The maximum error is recorded as under 6%. The results show that the current level of the flow uniformity can be ensured regardless of the volume flow rate with proper designs of the flow entrance structure. Table 6 shows the equivalent ratio of length to diameter for all the components adopted in the coolant path including straight sub-channel, flow distributing/combining structures, straight connecting tube, and U-type connecting tube. A considerable amount of friction loss occurs at the exit of the cooling plates, and U-type connecting tubes, which explains relatively larger pressure drop of type C with more number of the cooling plates and U-type tubes than other design types.

## References

[1] Manzetti S, Mariasiu F. Electric vehicle battery technologies: from present state to future systems. Renew Sustain Energy Rev 2015;1(51):1004–12.

[2] Zhao R, Zhang S, Liu J, Gu J. A review of thermal performance improving methods of lithium ion battery: electrode modification and thermal management system. J Power Sources 2015;20(299):557–77.

[3] Liu H, Wei Z, He W, Zhao J. Thermal issues about Li-ion batteries and recent progress in battery thermal management systems: a review. Energy Convers Manage 2017;15(150):304–30.

[4] Jaguemont J, Boulon L, Dubé Y. A comprehensive review of lithium-ion batteries used in hybrid and electric vehicles at cold temperatures. Appl Energy 2016;15(164):99–114.

[5] Feng X, Ouyang M, Liu X, Lu L, Xia Y, He X. Thermal runaway mechanism of lithium ion battery for electric vehicles: a review. Energy Storage Mater 2018;1(10):246–67.

[6] Wilke S, Schweitzer B, Khateeb S, Al-Hallaj S. Preventing thermal runaway propagation in lithium ion battery packs using a phase change composite material: an experimental study. J Power Sources 2017;1(340):51–9.

[7] Deng Y, Feng C, Jiaqiang E, Zhu H, Chen J, Wen M, et al. Effects of different coolants and cooling strategies on the cooling performance of the power lithium ion battery system: a review. Appl Therm Eng 2018;30(142):10–29.

[8] Han T, Khalighi B, Yen EC, Kaushik S. Li-ion battery pack thermal management: liquid versus air cooling. J Therm Sci Eng Appl 2019;11(2):021009.

[9] Zou D, Liu X, He R, Zhu S, Bao J, Guo J, et al. Preparation of a novel composite phase change material (PCM) and its locally enhanced heat transfer for power battery module. Energy Convers Manage 2019;15(180):1196–202.

[10] Lv Y, Situ W, Yang X, Zhang G, Wang Z. A novel nanosilica-enhanced phase change material with anti-leakage and anti-volume-changes properties for battery thermal management. Energy Convers Manage 2018;1(163):250–9.

[11] Wu W, Yang X, Zhang G, Ke X, Wang Z, Situ W, et al. An experimental study of thermal management system using copper mesh-enhanced composite phase change materials for power battery pack. Energy 2016;15(113):909–16.

[12] Xia G, Cao L, Bi G. A review on battery thermal management in electric vehicle application. J Power Sources 2017;1(367):90–105.

[13] Wu W, Wang S, Wu W, Chen K, Hong S, Lai Y. A critical review of battery thermal performance and liquid based battery thermal management. Energy Convers Manage 2019;15(182):262–81.

[14] Jarrett A, Kim IY. Design optimization of electric vehicle battery cooling plates for thermal performance. J Power Sources 2011;196(23):10359–68.

[15] Deng T, Zhang G, Ran Y. Study on thermal management of rectangular Li-ion battery with serpentine-channel cold plate. Int J Heat Mass Transf 2018;31(125):143–52.

[16] Zhang Y, Wang S, Ding P. Effects of channel shape on the cooling performance of hybrid micro-channel and slot-jet module. Int J Heat Mass Transf 2017;1(113):295–309.

[17] Huo Y, Rao Z, Liu X, Zhao J. Investigation of power battery thermal management by using mini-channel cold plate. Energy Convers Manage 2015;1(89):387–95.

[18] Lan C, Xu J, Qiao Y, Ma Y. Thermal management for high power lithium-ion battery by minichannel aluminum tubes. Appl Therm Eng 2016;25(101):284–92.

[19] Jin LW, Lee PS, Kong XX, Fan Y, Chou SK. Ultra-thin minichannel LCP for EV battery thermal management. Appl Energy 2014;1(113):1786–94.

[20] Chen D, Jiang J, Kim GH, Yang C, Pesaran A. Comparison of different cooling methods for lithium ion battery cells. Appl Therm Eng 2016;5(94):846–54.

[21] Chen K, Wu W, Yuan F, Chen L, Wang S. Cooling efficiency improvement of air-cooled battery thermal management system through designing the flow pattern. Energy 2019;15(167):781–90.

[22] Zhao C, Cao W, Dong T, Jiang F. Thermal behavior study of discharging/charging cylindrical lithium-ion battery module cooled by channeled liquid flow. Int J Heat Mass Transf 2018;31(120):751–62.

[23] Zhao C, Sousa AC, Jiang F. Minimization of thermal non-uniformity in lithium-ion battery pack cooled by channeled liquid flow. Int J Heat Mass Transf 2019;1(129):660–70.

[24] Shang Z, Qi H, Liu X, Ouyang C, Wang Y. Structural optimization of lithium-ion battery for improving thermal performance based on a liquid cooling system. Int J Heat Mass Transf 2019;1(130):33–41.

[25] Yeow K, Teng H, Thelliez M, Tan E. Thermal analysis of a Li-ion battery system with indirect liquid cooling using finite element analysis approach. SAE Int J Altern Powertrains 2012;1(1):65–78.

[26] Panchal S, Dincer I, Agelin-Chaab M, Fraser R, Fowler M. Experimental and theoretical investigations of heat generation rates for a water cooled LiFePO4 battery. Int J Heat Mass Transf 2016;1(101):1093–102.

[27] Vazquez-Arenas J, Gimenez LE, Fowler M, Han T, Chen SK. A rapid estimation and sensitivity analysis of parameters describing the behavior of commercial Li-ion batteries including thermal analysis. Energy Convers Manage 2014;1(87):472–82.

[28] Viswanathan VV, Choi D, Wang D, Xu W, Towne S, Williford RE, et al. Effect of entropy change of lithium intercalation in cathodes and anodes on Li-ion battery thermal management. J Power Sources 2010;195(11):3720–9.

[29] Gnielinski V. New equations for heat and mass transfer in turbulent pipe and channel flow. Int Chem Eng 1976;16(2):359–68.

[30] Karwa R, Solanki SC, Saini JS. Heat transfer coefficient and friction factor correlations for the transitional flow regime in rib-roughened rectangular ducts. Int J Heat Mass Transf 1999;42(9):1597–615.

[31] Pesaran A, Santhanagopalan S, Kim GH. Addressing the Impact of Temperature Extremes on Large Format li-ion Batteries for Vehicle Applications (presentation). Golden, CO (United States): National Renewable Energy Lab.(NREL); 2013.

[32] Pesaran AA. Battery thermal models for hybrid vehicle simulations. J Power Sources 2002;110(2):377–82.

[33] Panchal S, Dincer I, Agelin-Chaab M, Fraser R, Fowler M. Experimental investigation and simulation of temperature distributions in a 16Ah-LiMnNiCoO 2 battery during rapid discharge rates. Heat Mass Transf 2017;53(3):937–46.

[34] Hong EP, Kim DH, Choi KW, Ryu JC, Mun MS. Development of lithium polymer battery pack for powered wheelchair. Proceedings of the Korean Society of Precision Engineering Conference. Korean Society for Precision Engineering; 2013. p. 1191–2.

[35] Bergman TL, Incropera FP, DeWitt DP, Lavine AS. Fundamentals of Heat and Mass Transfer. John Wiley & Sons; 2011.

[36] Zhao J, Rao Z, Li Y. Thermal performance of mini-channel liquid cooled cylinder based battery thermal management for cylindrical lithium-ion power battery. Energy Convers Manage 2015;1(103):157–65.

[37] Rao Z, Wang Q, Huang C. Investigation of the thermal performance of phase change material/mini-channel coupled battery thermal management system. Appl Energy 2016;15(164):659–69.